Full length article

Formation mechanism of channel segregation in carbon steels by inclusion flotation: X-ray microtomography characterization and multi-phase flow modeling

Yan Fei Cao, Yun Chen[*], Dian Zhong Li

Shenyang National Laboratory for Materials Science, Institute of Metal Research, Chinese Academy of Sciences, Shenyang, Liaoning, 110016 PR China

A B S T R A C T

Recent experimental dissections of steel ingots and multi-scale simulations have led to the discovery of a potential driving force for channel segregation: the flotation of oxide-based inclusion (D. Li et al., Nat. Commun. 5:5572 (2014)). Further experimental analysis and numerical modeling are necessary to clarify this mechanism in detail. In this work, the inclusions in a carbon steel ingot that exhibits severe channel segregations were characterized by the 3D X-ray microtomography, which revealed a significant enrichment and growth of inclusions in the channels. Based on above microtomography characterization, a 2D macrosegregation model encompassing the inclusion flotation was established. In the model, the motions of solid inclusions and liquid were described using the multi-phase flow scheme within the Euler-Lagrange framework. The benchmark simulations showed that sufficient inclusion populations with appropriate sizes are capable of altering the local flow patterns and destabilize the mushy zone, initiating the subsequent channel segregation. The continuous interplay between melt convection, inclusion flotation and solidification eventually causes the formation of macroscale channel. The predicted sizes and volume fraction of inclusions that are able to trigger the channel segregation effectively are consistent with the data obtained via microtomography characterization. The macrosegregation model was then applied to predict the channel segregations in an industrial carbon steel ingot. A rather good agreement of A-segregates was achieved between the simulation and the dissected ingot.

© 2016 Acta Materialia Inc. Published by Elsevier Ltd. All rights reserved.

1. Introduction

As a typical kind of channel segregation, A-segregates are the most prevalent and notorious type of macrosegregation in casting steels and present as one of the main challenges facing the steel-maker at all stages of fabrication. They appear as the linear regions of chemical and even microstructure inhomogeneities, and form along a direction that is roughly antiparallel to gravity during solidification [1]. To understand and control their formation during solidification, a large amount of effort has been exerted for decades, including the theoretical analysis using Rayleigh number [2], experimental analysis using model alloys [3,4], numerical simulations based on the continuum model [5], the multi-phase/multi-scale model [6–11], the 3D microscale solidification model [12,13] and so on. With all of these studies, it is generally concluded that the thermosolutal convection induced by the density difference is the origin of channel segregation. In steels, accordingly, it is the sufficient buoyant force of the light interdendritic solute-enriched melt and the hotter liquid at the upper regions of mushy zone that jointly destabilize the mushy zone and cause the formation of A-segregates [2].

Nevertheless, it is frustrating that most of the simulations based on such a mechanism often failed to exactly predict the number, shape and locations of A-segregates in the industrial steel ingots. The failure is normally ascribed to the inputs of complex macrosegregation models, such as the coarsened computing grid, the uncertain material parameters and the simplification of auxiliary models [8,14–16]. However, recent investigations on macrosegregation in steels through a series of dissected steel ingots and multi-scale calculations which were performed by Li et al. [17] and then were highlighted by Plummer [18], have revealed a new mechanism of channel segregation formation. In the widely used steels with a high content of oxygen, they found that the flotation of light oxide-based inclusions is responsible for the formation of

* Corresponding author.
  E-mail address: chenyun@imr.ac.cn (Y. Chen).

Nomenclature

C_l, C_s, C	liquid, solid and mixture concentrations (wt.%)
h_s, h_l, H,	solid, liquid and mixture enthalpies (J kg^{-1})
ΔH	latent heat (J kg^{-1})
C^*	reference concentration (wt.%)
T^*	reference temperature (K)
u_p, v_p	particle velocity components in x and y directions (m s^{-1})
u, v	liquid velocity components in x and y directions (m s^{-1})
ua_p, va_p	average particle velocities in x and y directions (m s^{-1})
f_s, f_l	fractions of solid and liquid
$\vec{U}$	superficial velocity (m s^{-1})
$\vec{U_l}$	liquid velocity (m s^{-1})
λ	heat conductivity (W m^{-1} K^{-1})
c_p	specific heat (J kg^{-1}K^{-1})
μ_l	liquid dynamic viscosity (pa s)
$\vec{g}$	acceleration of gravity (m s^{-2})

n	particle number
m	liquidus slope (K wt.%$^{-1}$)
T_l, T_m	liquidus of steel and melting point of solvent (K)
d_s	secondary dendritic arm spacing (μm)
k	partition coefficient
f_p	area fraction of inclusion
β_T	thermal expansion coefficient (K^{-1})
β_C	compositional expansion coefficient (wt.%$^{-1}$)
Re	relative Reynolds number
ρ, ρ_p	densities of steel and inclusion (kg m^{-3})
P	pressure (pa)
d_p	particle diameter (m)
t	time (s)

Subscripts and Superscripts

s, l	solid and liquid phases
p	inclusion particle
i	the ith inclusion particle
sl, pl	interaction between liquid and solid or inclusion

channel segregation. The sufficient volume fraction of oxide-based inclusions with appropriate sizes can enhance the local flow, destabilize the mushy zone, and finally dominate the channel segregation formation. Obviously, this mechanism is quite different from the previous recognition of the driving force of channel segregation in solidifying steels.

Therefore, to address the effect of inclusions on channel segregation formation in depth, it is of great significance to establish a macrosegregation model incorporating the flow dynamics of inclusions. The previous multi-phase macrosegregation models that couple the settlement of dendritic or globular crystals are within the Euler–Euler category. Nevertheless, the light inclusion particles are different from these crystals, which are distributed in the melt dispersively and drag the surrounding melt moving together when they are floating upwards. Hence, their moving kinetics should be described within the Lagrange framework to accurately track the motion of each inclusion particle during solidification, as well as the dragging effect [19]. Actually, with the Lagrange approach a wide range of dispersed two-phase flow problems in metallurgy processes were investigated [20–24]. Based on the commonly used dispersed phase model for multiphase flow [20–24], an Euler-Lagrange flow model is incorporated into the conventional macrosegregation model in the current study.

In addition, the detailed examinations of the distributions and features of inclusions in the segregated channels can help further our understanding of the inclusion flotation mechanism in steels, as well as validate the simulation results. Hence, the inclusions in the A-segregate strips are characterized and determined carefully. Here, the three-dimensional X-ray microtomography technique [25,26] is applied to analyze the size, number and volume fraction of inclusions and pores. The theoretical basis of X-ray microtomography is the absorption contrasts between inclusions, pores and matrix. Compared with the conventional destructive metallographic techniques, the microtomography results are considered more reliable [27] because the drawbacks of the grinding and polishing processes during the preparation of samples can be ignored. More importantly, the distribution and morphology of inclusions in three-dimensional space can be visualized.

In this paper, the quantitative characterization of inclusions in carbon steels was first performed using the X-ray microtomography technique. A dispersed phase model that describes the motion of particles was then incorporated into the 2D continuum macrosegregation model. The effect of inclusions on the channel segregation in a benchmark cavity was analyzed in detail based on the developed model. Finally, the model was used to simulate the macrosegregation in a 500-kg 1045 steel ingot, particularly to reproduce the A-segregates that were observed in the dissected section.

2. 3D microtomography characterization of inclusions in the dissected 500-kg 1045 steel ingot

2.1. Experimental procedures

A 500-kg cylinder ingot of 1045 steel was first prepared and synthesized in a sand mould. The chemical compositions (wt.%) of the ingot are: C 0.47, Si 0.26, Mn 0.54, S 0.016, P 0.020, T.O (total oxygen content) 0.0056 and Fe balanced. The ingot dimensions and shape are illustrated in Fig. 1a. An insulation sleeve with a thickness of 40 mm was inserted at the circumference of the hot top sand mould. The top of the riser was covered by a 100 mm thick layer of covering flux. The steel was melted at 1873 K by an induction furnace and poured at 1823 K in the atmosphere after the Al-deoxidation process. The solidified as-cast ingot was cut in half along the longitudinal axis. After being ground and polished, the dissected center surface was etched in 5% aqueous nitric acid solution. Fig. 1b shows the final etched macrostructure of ingot body of which the top riser was cut away. The contrast generated by the etch in the optical microscopy is caused jointly by the contents of carbon, inclusions and even cavities. The darker positions always correspond to higher concentrations of them. With this contrast, severe segregated channels (A-segregates) can be clearly observed on both sides of the ingot body. Evidently, within the zones of A-segregates, besides the obvious positive carbon segregation, inclusions or even cavities can be observed to be converging together [17].

Then, the lab-based Xradia Versa XRM-500 system was used for 3D quantitative characterization of inclusions [28]. The resolution of the system can be as high as 0.7 μm. Three cylindrical samples with a dimension of Φ3 mm $\times$ 25 mm were cut from the non-channel zone, the bottom and body of the chosen segregated channel of the sectioned 1045 steel ingot as shown in Fig. 1b. The
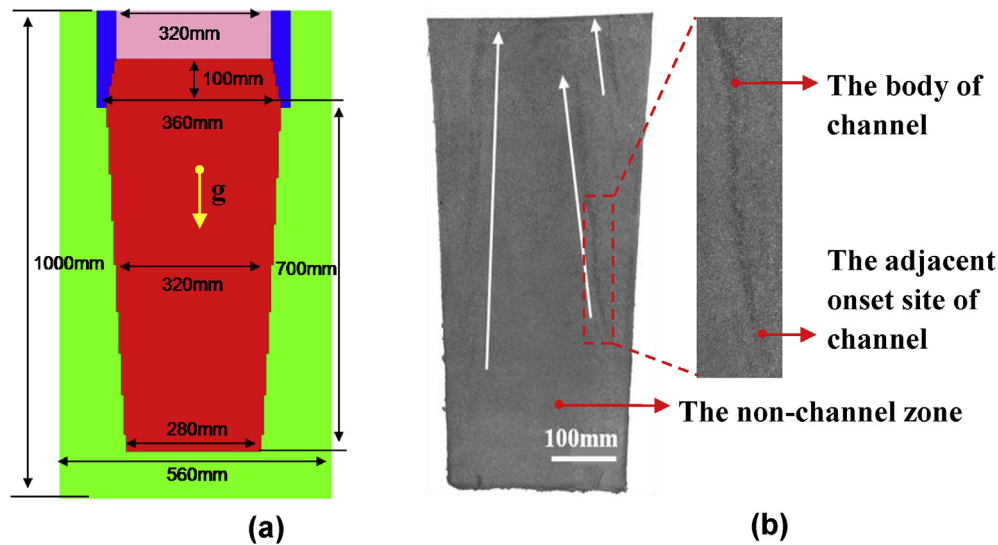
Fig. 1. (a) The section sketch and geometrical dimensions of the 500-kg 1045 steel ingot, in which the green, red, blue and pink regions denote the mould, ingot, insulation sleeve and covering flux, respectively. The yellow arrow denotes the gravity g. (b) the etched macrostructure of the longitudinal center surface, where A-segregates are marked with white arrows. A blown-up inset of a portion of the channel is inserted and the sample positions are also marked in (b). (For interpretation of the references to colour in this figure legend, the reader is referred to the web version of this article).

sample which locates at the bottom is adjacent to the onset site of the channel. Then, the samples underwent abrasive paper grinding and ultrasonic cleaning to ensure the cleaness. Finally, they were placed at the rotation stage of an X-ray tomography system with a working accelerating voltage of 140 kV. In total, for each sample 1600 projected images were recorded as the sample was rotated by 360°. The exposure time of each image is 4 s. The projections with a pixel size of approximately 3.5 μm was reconstructed via a filtered back projection algorithm, and then processed, visualized and computed using the software of Avizo fire 7.1. The background noise in the 3D data was removed using a median3d filter in the software to enhance the reliability of the information. The inclusion from the steel matrix was segmented using conventional threshold method according to the absorption contrast. The segmentation results were carefully checked on each slice of the whole 3D data. Here, it needs to be noted that inclusions with an equivalent diameter smaller than 4.34 μm cannot be detected in the current characterization. Moreover, because a particle that is made up of 1–2 voxels is most likely below the noise threshold of the reconstructed images, it is not reliable enough to resolve the inclusions below approximately 4 voxels, or an equivalent diameter of 8.68 μm. Therefore, the measured number of inclusion particles per unit volume, to some extent, will be thus reduced. However, this will not change the volume fraction dramatically. This is because most of the particles are in a diameter larger than 5 μm according to previous 2D microscopy characterization [17].

2.2. Inclusion measurements and observation

The measured inclusion dimension, population and morphology at the adjacent onset site and within the body of channel segregation are shown in Fig. 2. The 3D reconstructed regions in Fig. 2a and b are 1800 × 1460 × 2500 μm³ and 1750 × 1830 × 2260 μm³, respectively. The different colors represent the different equivalent volume diameters (each inclusion is considered as an equivalent sphere with a diameter d_p) of inclusions. As analyzed and identified by scanning electron microscopy (SEM) and energy dispersive spectra (EDS), the inclusions are composed mostly of Al_2O_3 and MnS [17]. In the sample adjacent to the onset site, the equivalent volume diameter of the inclusion is smaller than 100 μm, while in

the sample in the body of the channel, the largest diameter is 160 μm. In addition, it can also be seen from Fig. 2 that the inclusions in the body of the channel exhibit a larger volume fraction and population than that at the onset site. The comparisons of the inclusion distribution and quantity between them indicate that the inclusions tend to accumulate into the channel. Their morphologies also become more irregular and complicated with the evolution of channel segregation. These phenomena can be mainly ascribed to the following two facts. Firstly, after the initiation of the channel segregation, inclusions will coagulate and grow into a larger size during the development of the channel, owing to the weak wettability of Al_2O_3 particles. Secondly, the inclusions surrounding the path of channel can find their way to preferentially float into the channel together, eventually leading to the increments of inclusion quantity and dimension. By further summarizing the total volume of all inclusions, the volume fractions of inclusions at the adjacent onset site and within the body of channel segregation are approximately 0.09% and 0.35%, respectively.

Moreover, the quantitative statistical results of inclusions were summarized and compiled in Fig. 3. It shows that the equivalent volume diameters of most inclusions are at a range of 5–50 μm at both the onset site and body part of the channel, which is consistent with the 2D microscopy results [17]. Further, the number of inclusions with a diameter larger than 50 μm decreases with increasing size, but becomes obviously higher with the development of channel segregation compared to the onset site. The statistics also demonstrates that the volume fraction of inclusions with a diameter below 10 μm takes up a very small proportion. Hence, the specified resolution in the current characterization is reliable enough to resolve inclusions that contribute an effective driving force to channel segregation.

Fig. 4 further shows the characterized inclusions in the non-channel zone. In contrast, the sizes of inclusions in this zone are apparently smaller than that in the channel, most of which are less than 40 μm. The shape of inclusion is also more regular. In comparison with the inclusion distribution observed in the channel zone, they are distributed in the matrix more uniformly. The obtained total volume fraction of inclusions in the non-channel zone is approximately 0.07%, lower than that at the onset site and in the body of the channel zone.
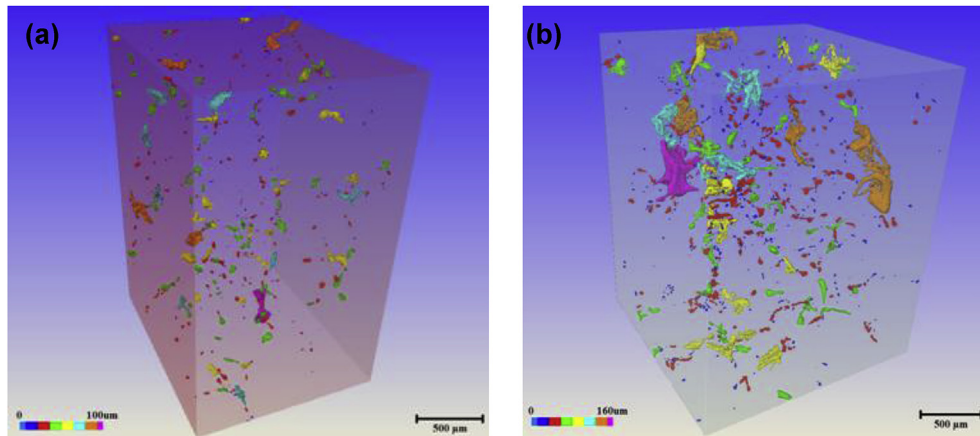
Fig. 2. The morphologies, dimensions and distributions of inclusions observed by 3D X-ray microtomography: (a) at the adjacent onset site, and (b) within the body part of the channel segregation in 1045 steel. The reconstructed dimensions of the left and right panels are $1800 \times 1460 \times 2500 \ \mu m^3$ and $1750 \times 1830 \times 2260 \ \mu m^3$, respectively.
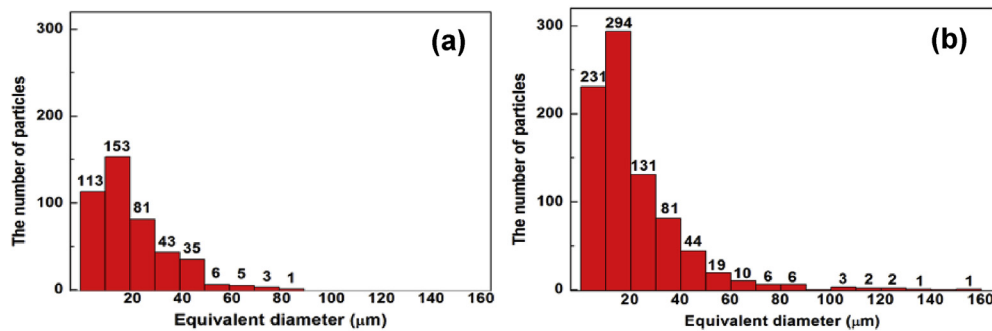

Fig. 3. The statistics on the number and dimensions of inclusions (a) at the adjacent onset site and (b) within the body part of the channel segregation in 1045 steel. The statistical regions are the same as those shown in Fig. 2.

Above characterization uncovers the accumulation of inclusions during the formation of channel segregation; nevertheless, the direct visualization of their evolution process is not possible by characterizing these fully solidified zones. However, the characterized results render the general concern that, the volume fraction of inclusions in the channel is so large that their influence on the melt flow should not be neglected. This concern becomes more crucial when bearing in mind that the moving dynamics of solid inclusion is very different from that of liquid. Therefore, in the following numerical simulations, the dynamic interactions between the solidification, natural convection and motion of inclusions during the formation of channel segregation in steels will be revealed.

3. Simulation methodology

In the current research, by coupling the multi-phase flow dynamics, a new two-dimensional macrosegregation model is built based on the classical continuum model. The fluid phase is treated as a continuum by solving the time-averaged Navier–Stokes
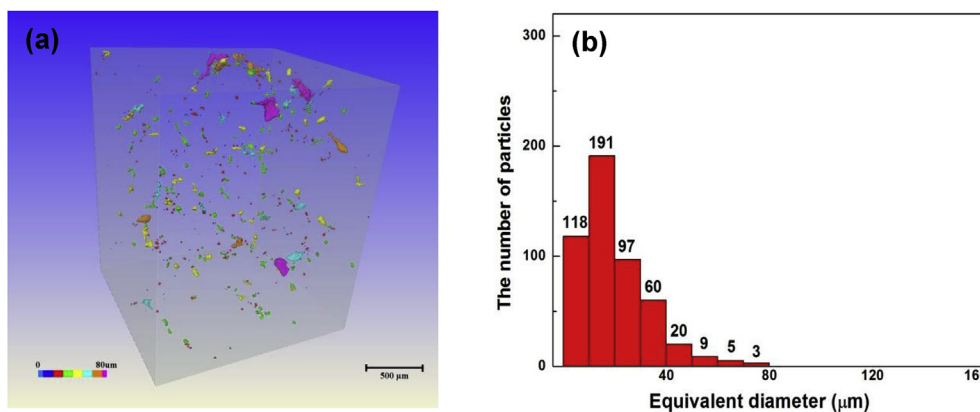

Fig. 4. The morphologies, dimensions and distributions of inclusions in the non-channel zone by 3D X-ray microtomography. (a) The 3D reconstructing image of inclusions, and (b) the statistical results of inclusions. The reconstructed dimensions of the left panel is $1700 \times 1880 \times 2260 \ \mu m^3$.

equations, solute and energy transport equations. The dispersed phase behavior is described by tracking the trajectories of a large number of inclusion particles during solidification in a Lagrangian reference frame. In addition, the two-way coupling approach is adopted to describe the interaction between the continuous and dispersed phases. The fluid phase will influence the particulate phase through the dragging effect and the latter disturbs the local melt convection through the source terms of momentum equations. Owing to the small volume fraction of inclusions in steels, the interaction between particles, such as direct particle collisions, is negligible. It should be stressed that, though the liquid solidified in three-dimensional space in experiment, the required finer mesh, jointly with the high computational cost of solving tridimensional convection, has deterred exploration in 3D simulation. In particular, the situation becomes tougher when coupling the motion of numerous inclusions. However, the predicted macrosegregation in two dimension showed no significant discrepancy from that in three dimension. The simulations performed by Carozzani et al. [29] indicated that the temperature distributions but in the edges of boundaries are almost the same via 2D and 3D simulations of Sn-3 wt.% Pb alloy in a benchmark cavity. The comparison between 2D and 3D calculations based on the two-phase columnar solidification model demonstrated that the segregation pattern on the center plane in the 3D case can be sufficiently reproduced by computationally inexpensive 2D calculations [30].

3.1. Continuum phase equations

The basic assumptions in the treatment of continuum phases are as follows. The solidified grains are supposed to be columnar. The effects of solid movement and shrinkage on macrosegregation are not taken into account except for thermosolutal natural convection. The liquid is Newtonian and incompressible while the convection is laminar. The effect of diffusion on the solute transport is also neglected. The main governing equations are described as follows, Conservation of mass (Continuity):

$$\nabla \cdot \left(\overrightarrow{U} \right) = 0 \tag{1}$$

Conservation of solute:

$$\frac{\partial [C]}{\partial t} + \nabla \cdot \left(\overrightarrow{U} C_l \right) = 0 \tag{2}$$

$$[C] = \int_0^{f_s} C_s d\alpha + f_l C_l \tag{3}$$

$$T_l = T_m + mC_l \tag{4}$$

Conservation of energy:

$$\frac{\partial (\rho H)}{\partial t} + \nabla \cdot \left(\rho \, c_p \overrightarrow{U} T + \rho \overrightarrow{U} \Delta H \right) = \nabla \cdot (\lambda \nabla T) \tag{5}$$

$$[\rho H] = f_s \rho_s h_s + f_l \rho_l h_l \tag{6}$$

Conservation of momentum (x and y directions):

$$\frac{\partial (f_l \rho \, u)}{\partial t} + \nabla \cdot \left(\rho \, \overrightarrow{U} u \right) = -f_l \frac{\partial P}{\partial x} + \nabla \cdot (\mu_l \nabla (f_l u)) + K_{sl}(u a_p - u)$$
$$+ \sum_{i=1} \left[K_{pl}^i \left(u_p^i - u \right) \right] \tag{7}$$

$$\frac{\partial (\rho f_l \, v)}{\partial t} + \nabla \cdot \left(\rho \, \overrightarrow{U} v \right) = -f_l \frac{\partial P}{\partial y} + \nabla \cdot (\mu_l \nabla (f_l v))$$
$$+ \rho \overrightarrow{g} f_l \left[\beta_T \left(T - T^* \right) + \beta_C \left(C_l - C^* \right) \right]$$
$$+ K_{sl}(v a_p - v) + \sum_{i=1} \left[K_{pl}^i \left(v_p^i - v \right) \right] \tag{8}$$

where $\overrightarrow{U} = f_l \overrightarrow{U_l}$ is the superficial velocity of liquid phase. To calculate the solid fraction, the same strategy was applied as that in Ref. [31] by solving the built quadratic equation considering the energy and species conservations, thermodynamic equilibrium at the solid–liquid interface and Scheil microsegregation model. K_{sl} (K^i_{pl}) is the interfacial friction coefficient between the solid dendritic network (the ith inclusion particle) and the fluid phase, which is modified from the Gidaspow correction [32].

$$K_{sl} = 150 \frac{f_s^2 \mu_l}{f_l d_s^2} \tag{9}$$

$$K_{pl}^i = \frac{3}{4} C_D \frac{f_p f_l \rho}{d_p} \left| v_p^i - v \right| f_l^{-2.65} \tag{10}$$

here, C_D is the drag coefficient and equal to $24/Re$ for spherical solid particles.

In addition, these governing equations are discretized on a staggered Cartesian mesh using a finite volume approach and uniform spaced grids. An explicit scheme of finite volume method is adopted to solve the coupled equations for temperature and concentration. The velocity-pressure coupling is realized using the SIMPLE algorithm. The iterated time step for the continuous phase is determined by the maximum fluid velocity at the previous time step. As the calculation of liquid flow is accomplished in a time step, the motion of inclusion is tracked via the following procedures.

3.2. Motion equations of dispersed phase

Based on the kinetics of particle motion, the moving velocity of a solid particle in melt depends on the buoyant force, gravity force and drag force. Considering that both the real inclusion size and quantity are small, it is reasonable to ignore some other forces acting on the particles, such as Brownian force, Saffman's lift force, virtue mass force and thermophoretic force [23]. Hence, the trajectory of each discrete particle is predicted by integrating the force balance on the particle. The motion of a spherical solid particle in the melt can be described as follows.

Velocity equations:

$$\frac{du_p^i}{dt} = \frac{18 \mu_l}{\rho_p d_p^2} \frac{C_D Re}{24} \left(u - u_p^i \right) \tag{11}$$

$$\frac{dv_p^i}{dt} = \frac{18 \mu_l}{\rho_p d_p^2} \frac{C_D Re}{24} \left(v - v_p^i \right) + \frac{\overrightarrow{g} (\rho_p - \rho)}{\rho_p} \tag{12}$$

Trajectory equations:

$$\frac{dx^i}{dt} = u_p^i, \quad \frac{dy^i}{dt} = v_p^i \tag{13}$$

where x^i and y^i are the displacements of the ith particle at time t in the x and y directions, respectively. The iterated time step for the dispersed phase is determined by the maximum particle velocity at the previous time step. Because Al_2O_3 is the main composition of

most inclusions, the inclusions are assumed as alumina in the current simulations. Hence, the density of particle, ρ_p, is equal to 3640 kg m^{-3} [33]. A solid particle will stop moving once it arrives at the domain boundaries or when it is blocked and engulfed by the fully developed dendritic network where the local solid fraction exceeds 0.5. The frictional force and floating velocity of each particle are significantly dependent on both its dimension and shape. A particle with an irregular shape will experience a larger frictional force than that with an ideal spherical shape. In the current simulations, to directly illustrate the effects of the particle size on the liquid flow and formation of channel segregation, all the particles are assumed to have an ideal circular shape in two dimension with the same diameter. The agglomeration and growth of particles are not considered.

To investigate the influence of inclusions on the channel segregation formation in plain carbon steels, numerical simulations in Fe-0.36 wt.% C have been performed with different sizes and initial number of particles. The lateral solidifications in a Hunt-Benchmark cavity (100 mm × 60 mm) were simulated, where the cavity was cooled down from the right-hand side and the remaining sides were thermally insulated as sketched in Fig. 5. The initial temperature is the liquidus temperature. The heat transfer coefficient between heat-extraction side and atmosphere is 300 W m^{-2} K^{-1}, which is referred from other model alloy systems such as Sn–Pb alloy [34,35]. The main physical parameters of the steel are listed in Table 1 according to Ref. [8]. The mesh size is 1 mm × 1 mm. Previous simulations have shown that the simulated results do not vary with a finer mesh [36]. In addition, to reproduce the channel segregation in an actual steel ingot with the developed multi-phase flow model, corresponding simulations of the experimental 500-kg 1045 steel ingot with a grid size of 5 mm × 5 mm were also carried out. The alloy properties of Fe-0.45 wt.% C system can be referred to Table 1 except d_s, which is selected as 500 μm according to the experimental result. The necessary initial and thermal conditions are also listed in Table 2.

4. Numerical simulation results and discussion

4.1. The influences of inclusion size and quantity on the channel formation

The simulations were first performed to illustrate the influence of the particle diameter on the channel segregation. Fig. 6 shows the final carbon distributions and segregation patterns with the inclusion particle diameters ranging from 2 to 50 μm in Fe-0.36 wt.% C system. In the simulations, 500 initial particles with zero velocity were injected into the cavity randomly at the

Table 1
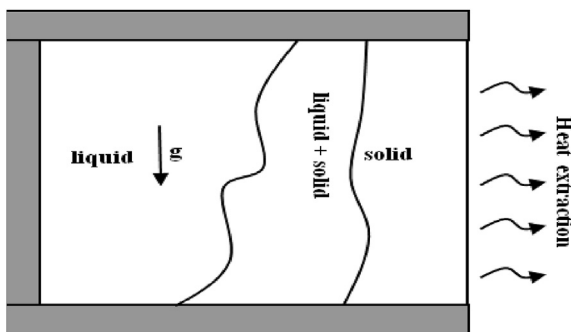Main physical parameters of Fe-0.36 wt.% C in benchmark simulations.

| Symbol	Unit	Value
ρ	kg m^{-3}	6990
k		0.314
m	K wt.%$^{-1}$	−80.45
T_m	K	1805
ΔH	J kg^{-1}	2.71×10^5
C_p	J kg^{-1} K^{-1}	500
d_s	μm	100
λ	W m^{-1} K^{-1}	39.3
β_T	K^{-1}	1.07×10^{-4}
β_C	wt.%$^{-1}$	1.4164×10^{-5}
μ_l	Pa s	4.2×10^{-3}

beginning of solidification. From Fig. 6a, it can be seen that as the particle size is very small, no obvious channel segregations appear but lots of isolated small zones with a little higher concentration are disorderly dispersed in the cavity. With an increase in the diameter of the particle, such kinds of small zones tend to accumulate into a line at the early stage of solidification and to connect each other. As the diameter is increased up to 10 μm, very obvious chains form at the upper-right corner of the domain, namely the channel segregations. However, unexpectedly, when the particle size increases to a sufficiently large size, i.e., a diameter larger than 20 μm, the segregated channels diminish again and even disappear without any solute enriched zones left in the broad central region of the domain as seen in Fig. 6g. It was further found that inclusions with a size ranging from 5 to 30 μm are capable of driving the formation of final macroscale channel segregation. This is because when the particles are too small (i.e., less than 5 μm), they will float weakly and slowly and drift with the current of thermosolutal convection or be easily captured by the relatively fast moving solid [17]. Consequently, most of the injected small inclusion particles will distribute irregularly and separately. Nevertheless, because the light inclusion tends to move upward in the direction of solute-dominated flow along the mushy zone, the natural convection is thus strengthened, which changes the solute concentration locally. As a result, lots of small solute enriched zones form at the region a little far away from the bottom wall as shown in Fig. 6a.

Yet when the particles are too large (i.e., larger than 30 μm), they will float quickly towards the top, driven by the strong buoyant force. In the case of Fig. 6g, after solidifying for 15 s, almost all particles accumulate near the upper wall. At this time, the solidified zone is less than 5%. Although the dragged liquid flow velocity is much stronger than the convection induced by the thermosolutal buoyancy, the perturbations of particles on the melt flow are instantaneous and vanish quickly before the melt starts or continues to freeze. Hence, the influence of these large particles on the mushy zone is only limited to the solidified zones formed early, where the particles have not already moved away to the upper boundary. Owing to the absence of inclusions as the solidification progresses further into the bulk melt, the interactions between particles and the mushy zone do not last for a long time, and therefore are not able to trigger the occurrence of channel segregation. Coincidentally, the effective sizes of inclusions obtained in the simulations are in accordance with the results of the 3D tomography characterization of inclusions in the channel zones, where most of inclusions are in the diameters of 5–50 μm. Because of the blocking of the complex dendritic structures in the real solidification and the rough shape of inclusions, the effective sizes of inclusions should be larger than that in simulations. Moreover, the agglomeration and growth of particles during and after the formation of channel segregation will also raise the inclusion size, which has been neglected in the present simulations.

Fig. 5. Schematic of solidification configuration in the current simulations of Hunt-Benchmark cavity (100 × 60 mm^2) cooling from the right-hand side, and the grey regions denote adiabatic walls.

Table 2
The initial and thermal conditions in the simulations of 500-kg 1045 steel ingot.

Material/Property	ρ (kg m^{-3})	C_P (J kg^{-1} K^{-1})	λ (W m^{-1} K^{-1})
Sand mould	1520	1070	0.73
Insulation sleeve	600	1130	0.2
Covering flux	210	400	0.18
Interfacial heat transfer coefficient	Ingot and covering flux: 300		
(W m^{-2} K^{-1})	Ingot and sand mould: 500		
	Ingot and insulation sleeve: 200		
	Covering flux and the outside: $5 + 4 \times 5.67 \times 10^{-8} \times \varepsilon \times T^3$, $\varepsilon = 0.5$		
	Sand mould and the outside: $10 + 4 \times 5.67 \times 10^{-8} \times \varepsilon \times T^3$, $\varepsilon = 0.9$		
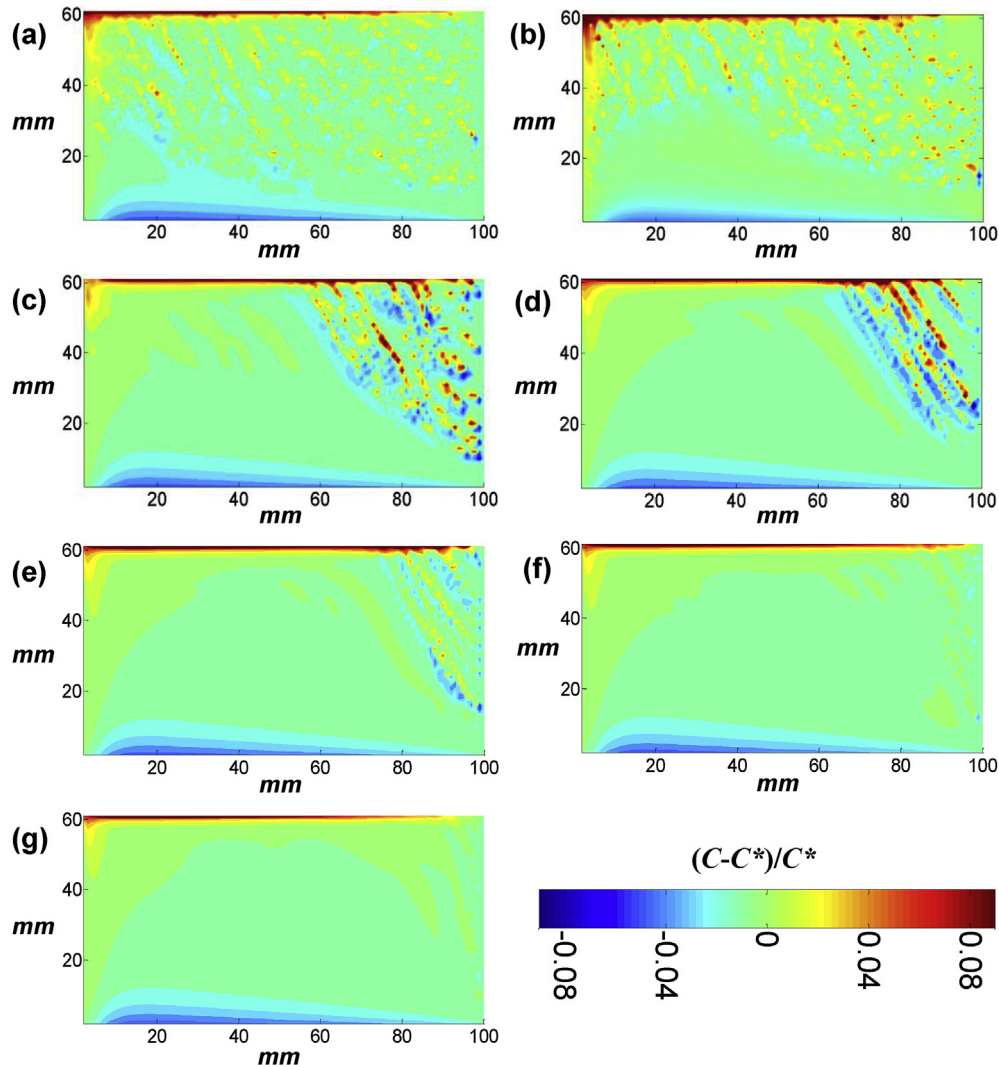
Fig. 6. The final relative segregation contours of carbon and channel distributions in the whole domain with various particle diameters d_p of (a) 2, (b) 5, (c) 10, (d) 15, (e) 20, (f) 30 and (g) 50 μm.

The provocation of channel segregation not only depends on the size of inclusions but also closely depends on their population. To quantify the effect of inclusion quantity, in the following simulations the initial particle numbers were set to 100, 500 and 1000, while the particle diameter was fixed at 10 or 15 μm. The simulated carbon distributions are shown in Fig. 7. It can be clearly seen that when 100 inclusion particles with a diameter of 10 μm were injected into the melt, no channels would form except for the formation of some localized zones with highly concentrated carbon (Fig. 7a1). With an increasing quantity of particles, the channel

segregations become more and more severe. Meanwhile, the number of channels is also apparently elevated. By comparing the channel segregations induced by the different diameters of inclusions, the results indicate that when the diameter of the inclusions is larger, the quantity required to induce distinct channels can be smaller. These varying trends of segregations with the quantity and size of inclusion particles can be analyzed and interpreted from two aspects. On the one hand, with an increase of the size of the initial particles the disturbance to interdendritic convection is enhanced because of the larger inclusion flotation force
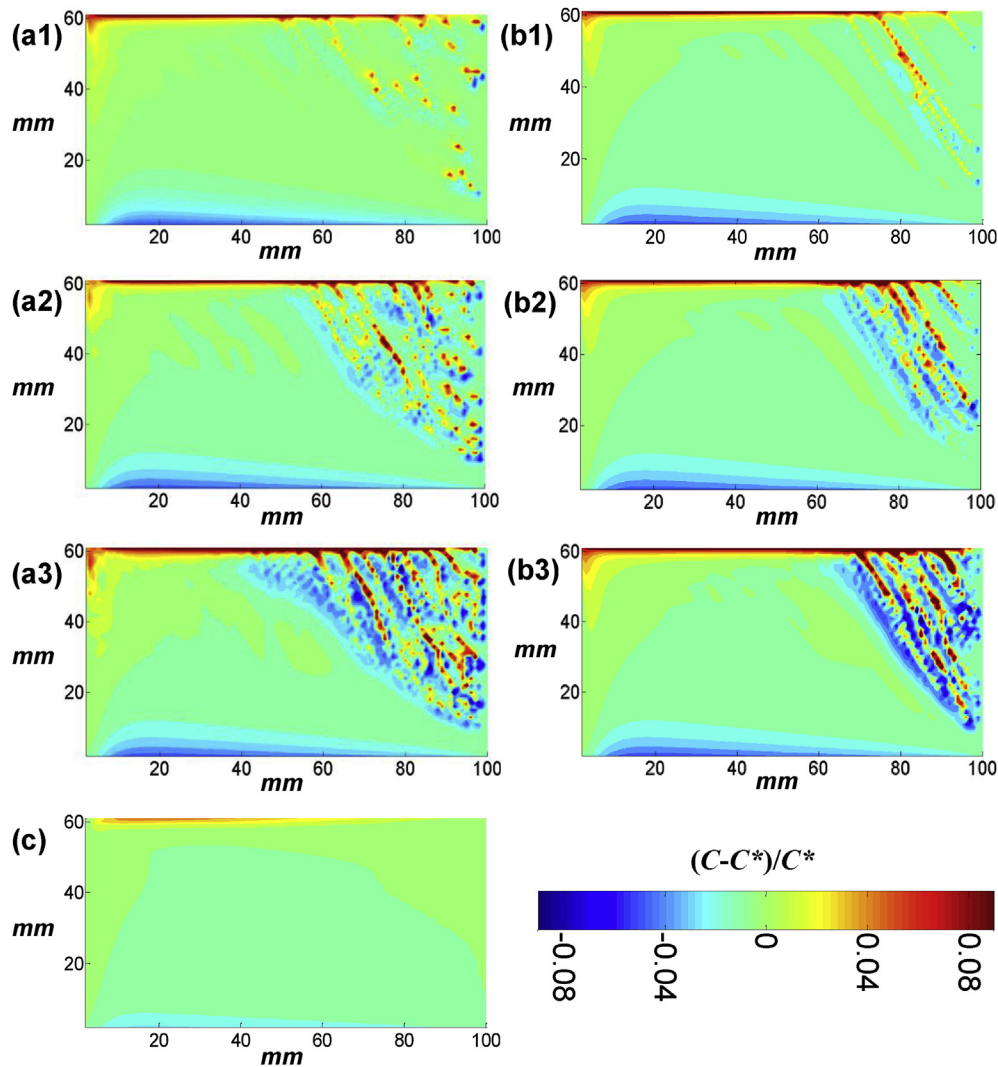
Fig. 7. The final relative segregation contours of carbon and channel distributions in the whole domain with various particle numbers of (a1, b1) 100, (a2, b2) 500 and (a3, b3) 1000; (c) the inclusion-free effect on channel segregation. In (a1-a3) and (b1-b3) d_p are 10 and 15 μm, respectively.

driven by more locally concentrated inclusion particles. Meanwhile, affected by the local drastic convection dragged by the inclusions, more solutes will also segregate. In addition to these floating inclusions and surrounding solute-rich melts, some of the adjacent inclusions on the way will also enter the triggered channel, which further reinforces this disturbance. On the other hand, increasing the quantity of the initial particles does increase the probability of destabilizing the mushy zone. That is, the mushy zone destabilization can be triggered at more sites simultaneously. As a result, more channels will appear eventually. By further calculations, the sufficient volume fraction of the inclusions to induce the channel segregation in the local mushy zone has been estimated in the order of magnitude of ~0.01%. This critical volume fraction is close to the measured values at the onset site and non-channel zone of the 500-kg steel ingot.

By contrast, Fig. 7c also gives the final carbon contour map without considering the effect of inclusions. As expected, no channel segregation can be formed just by the thermosolutal convection. In addition, it can be clearly seen that both the positive segregation near the upper side and the negative segregation at the bottom side are elevated obviously when taking into consideration the inclusion effect.

4.2. The evolution and formation of channel segregation induced by inclusion flotation

The formation of channel segregation is a result of the interactions between solidification, thermosolutal convection and inclusion flotation [17]. By carefully analyzing the evolutions of solute distributions, inclusion trajectories, flow fields and solid fraction isolines during solidification, we found that the formation of channel segregation driven by inclusion flotation could generally be divided into two stages: channel initiation and channel growth. It should be stressed that these two stages are similar to the formation process of the channel segregation merely driven by the thermo-solutal convection as described by Li and coworkers [10,37]. Fig. 8 shows the comparisons of these fields between simulations with and without consideration of inclusion flotation after solidification for 65 s. In Fig. 8c and d the particle diameter is 15 μm and its number is 500.

When the inclusions are absent in the simulation, only a single convective vortex results from the thermosolutal buoyancy in the bulk liquid and mushy zone. The convection keeps this stable flow pattern until the solidification ends. The isolines of solid fraction are straight without any deformation, as demonstrated in Fig. 8b.

Unlike the obvious channel segregation formation in the simulations of common model alloys (i.e., Sn–Pb, Sn–Bi, Al–Cu, Ga–In and Ni-based superalloy) under the same solidification conditions [36], no channel segregation is observed in the present simulations. This is because of the rather weak convection caused by the low amount of solute in Fe-0.36 wt.% C. In the model alloys, the solute content is at least one order of magnitude higher, and the consequent convection is so strong that it can deform the mushy zone and result in the channels [36]. When the inclusions are introduced, the flow pattern and solidification mode change distinctly. Owing to the light density of inclusions, they float upwards spontaneously. During their flotation, they drag the surrounding melt moving together, thereby strengthening the local fluid flow and even changing the flow direction. Because the inclusions are randomly distributed in the melt initially, the flow becomes very chaotic, particularly at the upper region of the cavity as solidification progresses for a while, as shown in Fig. 8d. This flow pattern is quite different from that in Fig. 8b. The localized increase of flow velocity near the mushy zone alters the solute transport and the subsequent solidification, which consequently causes the local solute segregation and restrains the local solidification. Hence, the advancing rate of the mushy zone varies spatially. This is characterized by the rather wavy isolines of solid fraction as displayed in Fig. 8d. With the help of inclusion flotation, the mushy zone starts to deform, and the channel is initiated.

However, the macroscale channel cannot be formed without successive deformation of the mushy zone by the inclusions. To sustain the progress of the initiated channel, the moving velocity of the particles and the solidification rate of the melt should be synchronous or sufficient amounts of inclusions always exist during the advancing of the mushy zone. For the former case, the inclusion floating velocity is mainly determined by its own dimension, so that for a given solidification condition, the size of particle should be in an appropriate range to progress the channel segregation. For the latter case, because the formation and growth of small inclusions are ignored in the present simulations, sufficient amount of large-size solid particles are necessitated to be supplied in the mushy zone in the early stage of solidification. In either case, after a segregated channel is initiated, the particles in the channel will preferentially float incline-upwards due to the thermal field. With further particle flotation and solidification, particles will not only drag the surrounding solute-rich melts flowing together but also cause the enrichment of adjacent particles. All of these processes and phenomena can ensure that the interactions between particles and solidification last for a long period, and thus the flow instability and mushy zone destabilization will continue until the macroscale channel eventually forms. These evolution processes can be observed by tracking the particle distributions and solidification behavior from 15 to 65 s as shown in Fig. 9. From the figure, it can be seen that the particle distributions appear in a line almost parallel to the channels with concentrated solutes, as indicated by the green-dashed arrows. Here, it is worth noting that because the solidification microstructure is much more complex in the real solidification of ingot than the simulated shape of mushy zone, the
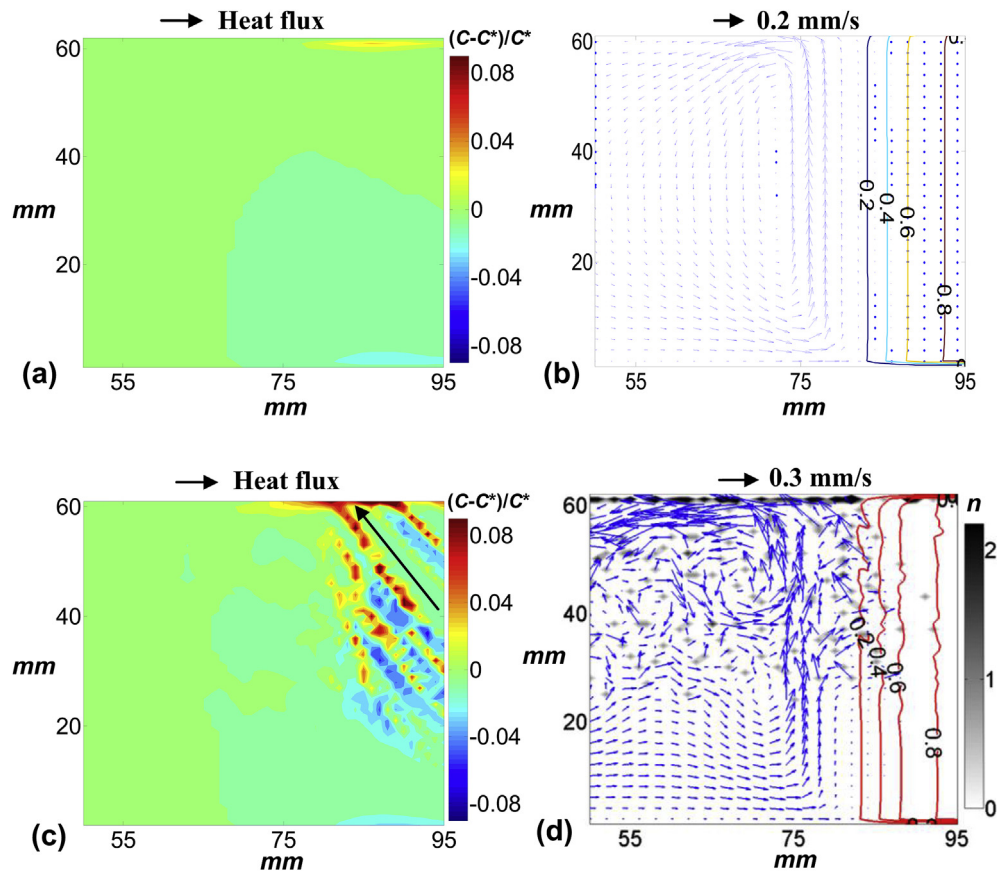

Fig. 8. The fluid velocity, solid fraction, carbon or/and inclusion distributions at the local selected zone after solidified for 65 s (a) and (c) are the relative carbon segregation contours without and with considering inclusion effects, respectively. (b) and (d) are the flow field and solid fraction isolines distributions without and with considering inclusion effects, respectively, and in (d) the particle distributions are superimposed. The detailed evolution of the chosen channel marked by the black arrow in (c) is shown in Fig. 9. The legend on the right of (d) shows the number n of particles in each cell.

inclusion will act on the mushy zone in a much more complicated way, such as the blocking by the dendritic network, eroding the dendritic branches and adsorbing low melting elements together to remelt solid.

4.3. Comparison of channel segregation between simulation and experimental results in an industrial steel ingot

To reproduce the A-segregates observed in the dissected ingot shown in Fig. 1b, the developed multi-phase flow model was then applied to simulate the macrosegregation in a 500-kg Fe-0.45 wt.% C steel ingot. In terms of the ingot symmetry and computational efficiency, half of the ingot was simulated. The cooling conditions are different from the previous unidirectional solidification in a benchmark cavity. Heat is extracted from all the sides contacting with the atmosphere as that in the experiment. The diameter of the injected particles was set equal to the averaged particle diameter in the region adjacent to the onset site of the channel segregation, which approximates to 30 μm. The number of particle was chosen to be 10000. This number is still smaller than that estimated from the dissected ingot but is almost the upper limit of computing time that can be acceptable. Simulations with a number ranging from 10 to 10000 showed that, as the population is larger than 500, the evolution trend of channel segregations are almost the same except for the longer channels and more severe solute segregation. Fig. 10c shows the carbon segregation contours of the ingot after solidification. As a comparison, the simulated result without considering the effect of inclusion is also presented in Fig. 10a.

As the inclusion effect is excluded in the simulation, the final solidified ingot is featured with the upper positive segregation, bottom negative segregation and two slices of channel segregations at the side of the top riser. These characteristics are generally consistent with the predicted results by Combeau et al. [8] and Li

et al. [38]. The slight channels appearing occasionally in the riser may be closely related to the abrupt changes of insulation and geometry conditions at the junction of the riser and the ingot body, where the complex flow field is beneficial to destabilizing the mushy zone. Similar to the already reported simulations of industrial steel ingots [7,38,39] and previous benchmark simulation without considering the inclusions, the A-segregates are also not observed here. However, after introducing the inclusion particles to the melt, the final macrosegregation patterns are dramatically changed. From Fig. 10c, it can be seen that besides the similar positive and negative segregations, which appear in Fig. 10a, there are several channels, which stem from the side of lower part of the ingot and then extend to incline-up until they reach the riser. Because of the distinct cooling conditions and geometrical shape of the 500-kg ingot, the orientations of channel segregations appear to be quite different from previous benchmark simulations. Surprisingly, the position and shape of these channel segregations show a very good agreement with the A-segregates appearing in the etched section surface of the experimental ingot body that is shown in Fig. 10b. Therefore, these comparison results demonstrated that the inclusion flotation is the dominating driving force for the formation of A-segregate in carbon steels, which also accounts for its disappearance in most previous simulations of large industry-scale steel ingots.

5. Conclusions

Detailed 3D microtomography characterization of inclusions in the channel and non-channel zones of a steel ingot has been carried out to illustrate the mechanism of channel segregation by inclusion flotation in carbon steels in detail. The examined equivalent diameters of inclusions are in a range of 5−50 μm, and the inclusion volume fractions at the adjacent onset site and within the body of
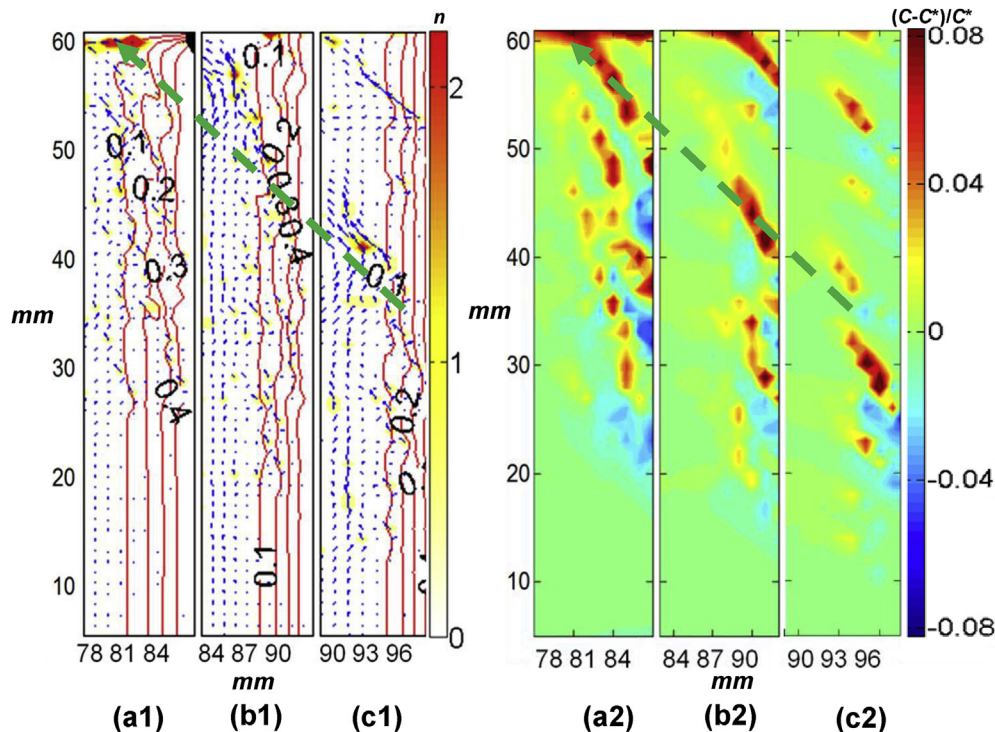

Fig. 9. The channel segregation evolution induced by inclusion flotation during solidification of 15−65 s (a1-c1) are the part of flow filed, solid fraction isolines and particle distributions in the mushy zone at 65, 35 and 15 s, respectively; (a2-c2) show the corresponding carbon distributions. The green-dashed arrows denote the developing trajectory of the chosen channel in Fig. 8c. (For interpretation of the references to colour in this figure legend, the reader is referred to the web version of this article).
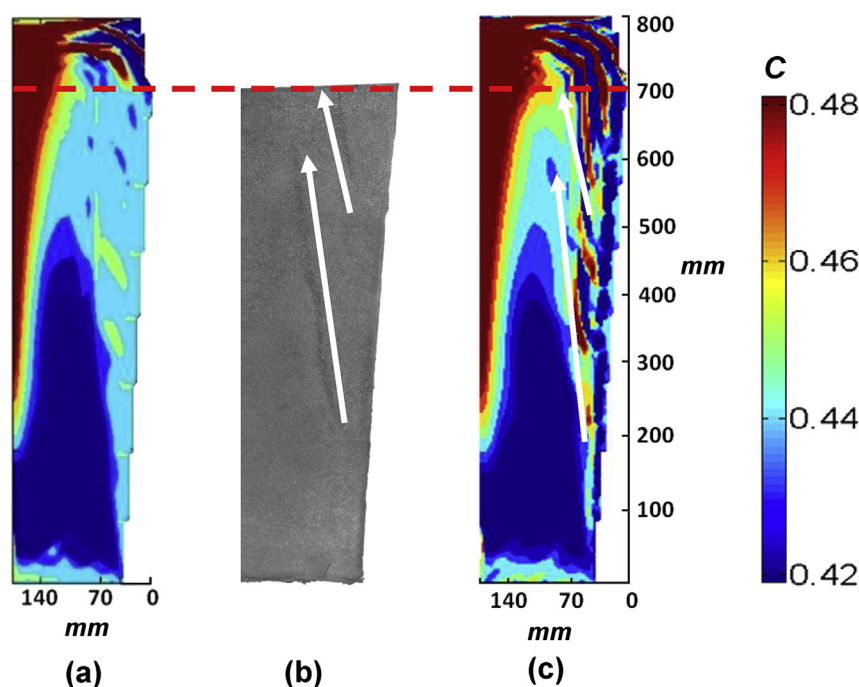
Fig. 10. The comparison of channel segregation in Fe-0.45 wt.% C system between simulation and experimental results of the industrial 500-kg 1045 steel ingot: the predicted results of (a) without and (c) with considering the inclusion effects, respectively; (b) the etched result of channel segregations. The white arrows denote the segregated channels. The top riser of the ingot had been cut away before etching.

channel segregation average approximately 0.09% and 0.35%, respectively, whereas in the non-channel zone, the fraction is lower. The characterization reveals the enrichment of inclusions into the channels and their growth. Hence, the dynamics and evolution of inclusions during the formation of channel segregation should not be ignored.

In terms of the characterized results, a new two-dimensional macrosegregation model coupling the multi-phase flow dynamics has been developed to elaborate the interaction between inclusion flotation and solidification. Based on this model, the initiation conditions, evolution and forming mechanism of channel segregation induced by inclusion flotation have been investigated in the Fe-0.36 wt.% C alloy solidified in a benchmark cavity. The simulations revealed that sufficient population of inclusions with appropriate diameters are able to alter the local flow pattern and destabilize the mushy zone, consequently initiating the channel segregation. Then, with the aid of enriched solutes and adjacent inclusions, the interactions between inclusions and mushy zone will be maintained until the final formation of macroscale channel. To trigger the occurrence of channel segregation, the inclusion volume fraction should be at least ~0.01% order of magnitude and the diameter should be within 5–30 μm, which are in the range that was measured in the experiment.

The established model is employed to simulate the formation of A-segregates in an industrial steel ingot. Through the simulations of a 500-kg 1045 steel ingot and comparison with the dissected result, the shape and position of A-segregates can be well reproduced when the inclusion flotation effects are taken into account. Meanwhile, the other types of macrosegregation are almost the same as the simulations while considering only the thermosolutal buoyancy. Hence, these results convince us that the inclusion flotation plays a crucial role in the formation of A-segregates in carbon steels.

References

[1] E.J. Pickering, H.K.D.H. Bhadeshia, Macrosegregation and microstructural evolution in a pressure-vessel steel, Metall. Mater. Trans. A 45 (2014) 2983–2997.
[2] M.T. Rad, P. Kotas, C. Beckermann, Rayleigh number criterion for formation of A-segregates in steel castings and ingots, Metall. Mater. Trans. A 44 (2013) 4266–4281.
[3] S.M. Copley, A.F. Giamei, S.M. Johnson, M.F. Hornbecker, The origin of freckles in unidirectionally solidified castings, Metall. Trans. 1 (1970) 2193–2204.
[4] R. Mehrabian, M. Keane, M.C. Flemings, Experiments on macrosegregation and freckle formation, Metall. Trans. 1 (1970) 3238–3241.
[5] W.D. Bennon, F.P. Incropera, The evolution of macrosegregation in statically cast binary ingots, Metall. Trans. B 18 (1987) 611–616.
[6] C.Y. Wang, C. Beckermann, Equiaxed dendritic solidification with convection.1, Multiph. Model. Metall. Mater. Trans. A 27 (1996) 2754–2764.
[7] M. Wu, A. Ludwig, A three-phase model for mixed columnar-equiaxed solidification, Metall. Mater. Trans. A 37 (2006) 1613–1631.
[8] H. Combeau, M. Zaloznik, S. Hans, P. Richy, Prediction of macrosegregation in steel Ingots: influence of the motion and the morphology of equiaxed grains, Metall. Mater. Trans. B 40 (2009) 289–304.
[9] M. Wu, A. Ludwig, Modeling equiaxed solidification with melt convection and grain sedimentation-I: model description, Acta Mater 57 (2009) 5621–5631.
[10] J. Li, M. Wu, A. Ludwig, A. Kharicha, Simulation of macrosegregation in a 2.45-ton steel ingot using a three-phase mixed columnar-equiaxed model, Int. J. Heat. Mass Transf. 72 (2014) 668–679.
[11] M. Ahmadein, M. Wu, A. Ludwig, Analysis of macrosegregation formation and columnar-to-equiaxed transition during solidification of Al-4wt.%Cu ingot using a 5-phase model, J. Cryst. Growth 417 (2015) 65–74.
[12] L. Yuan, P.D. Lee, A new mechanism for freckle initiation based on microstructural level simulation, Acta Mater 60 (2012) 4917–4926.
[13] S. Karagadde, L. Yuan, N. Shevchenko, S. Eckert, P.D. Lee, 3-D microstructural

model of freckle formation validated using in situ experiments, Acta Mater 79 (2014) 168–180.

[14] E.J. Pickering, Macrosegregation in steel ingots: the applicability of modelling and characterisation techniques, ISIJ Int. 53 (2013) 935–949.

[15] C. Beckermann, Modelling of macrosegregation: applications and future needs, Int. Mater. Rev. 47 (2002) 243–261.

[16] A. Kumar, B. Dussoubs, M. Založnik, H. Combeau, Influence of discretization of permeability term and mesh size on the prediction of channel segregations, IOP Conf. Ser. Mater. Sci. Eng. 27 (2012) 012039.

[17] D. Li, X-Q. Chen, P. Fu, X. Ma, H. Liu, Y. Chen, Y. Cao, Y. Luan, Y. Li, Inclusion flotation-driven channel segregation in solidifying steels, Nat. Commun. 5 (2014) 5572.

[18] J. Plummer, Homogenized steel, Nat. Mater 14 (2015) 13.

[19] A. Kitagawa, Y. Murai, F. Yamamoto, Two-way coupling of Eulerian–Lagrangian model for dispersed multiphase flows using filtering functions, Int. J. Multiphas Flow. 27 (2001) 2129–2153.

[20] N.A. Lebedeva, A combined fully lagrangian approach to modeling two-phase dispersed flows, Dokl. Phys. 58 (2013) 244–248.

[21] B.G. Thomas, Q. Yuan, S. Mahmood, R. Liu, R. Chaudhary, Transport and entrapment of particles in steel continuous casting, Metall. Mater. Trans. B 45 (2013) 22–35.

[22] Y. Wang, L. Zhang, Fluid flow-related transport phenomena in steel slab continuous casting strands under electromagnetic brake, Metall. Mater. Trans. B 42 (2011) 1319–1351.

[23] Lebanon, NH, FLUENT 6.3, User Manual, Ansys Inc., 10 Cavendish Court, 2006.

[24] Q. Yuan, B.G. Thomas, S.P. Vanka, Study of transient flow and particle transport in continuous steel caster molds-part II. particle transport, Metall. Mater. Trans. B 35 (2004) 703–714.

[25] S.R. Stock, X-ray microtomography of materials, Int. Mater. Rev. 44 (1999) 141–164.

[26] S.R. Stock, Recent advances in X-ray microtomography applied to materials, Int. Mater. Rev. 53 (2008) 129–181.

[27] R.W. Hamilton, M.F. Forster, R.J. Dashwood, P.D. Lee, Application of X-ray tomography quantify the distribution of TiB_2 particulate in aluminium, Scr.

[28] S. Wang, S. Wang, L. Zhang, Application of high resolution transmission X-ray tomography in material science, Acta Metall. Sin. 49 (2013) 897–910.

[29] T. Carozzani, C.A. Gandin, H. Digonnet, M. Bellet, K. Zaidat, Y. Fautrelle, Direct simulation of a solidification benchmark experiment, Metall. Mater Trans. A 44 (2012) 873–887.

[30] J. Li, M. Wu, J. Hao, A. Ludwig, Simulation of channel segregation using a two-phase columnar solidification model–Part I: Model description and verification, Comput. Mater. Sci. 55 (2012) 407–418.

[31] D. Liu, B. Sang, X. Kang, D. Li, Effect of alloy insert on channel segregation during solidification of Sn-10 wt pct Bi alloy, Metall. Mater. Trans. B 42 (2011) 210–223.

[32] D. Gidaspow, Multiphase Flow and Fluidization: Continuum and Kinetic Theory Description, Academic Press, New York, 1994.

[33] H. Shibata, D.R. Poirier, T. Emi, Modeling the behavior of Al_2O_3 inclusions during the dendritic solidification of steel, ISIJ Int. 38 (1998) 339–347.

[34] N. Ahmad, J. Rappaz, J.L. Desbiolles, T. Jalanti, M. Rappaz, H. Combeau, G. Lesoult, C. Stomp, Numerical simulation of macrosegregation: a comparison between finite volume method and finite element method predictions and a confrontation with experiments, Metall. Mater. Trans. A 29 (1998) 617–630.

[35] A. Kumar, B. Dussoubs, M. Založnik, H. Combeau, Effect of discretization of permeability term and mesh size on macro- and meso-segregation predictions, J. Phys. D. Appl. Phys. 42 (2009) 105503.

[36] Y. Cao, Y. Chen, D. Li, H. Liu, P. Fu, Comparison of channel segregation formation in model alloys and steels via numerical simulations, Unpublished results..

[37] J. Li, M. Wu, J. Hao, A. Kharicha, A. Ludwig, Simulation of channel segregation using a two-phase columnar solidification model-Part II: mechanism and parameter study, Comput. Mater. Sci. 55 (2012) 419–429.

[38] W. Li, H. Shen, X. Zhang, B. Liu, Modeling of species transport and macrosegregation in heavy steel ingots, Metall. Mater. Trans. B 45 (2014) 464–471.

[39] J.P. Gu, C. Beckermann, Simulation of convection and macrosegregation in a large steel ingot, Metall. Mater. Trans. A 30 (1999) 1357–1366.